

# Effects of line-tying on resistive tearing instability in slab geometry

Yi-Min Huang<sup>1,2,\*</sup> and Ellen G. Zweibel<sup>1,2,3,†</sup>

<sup>1</sup>*Center for Magnetic Self-Organization in Laboratory and Astrophysical Plasmas,  
University of Wisconsin, Madison, Wisconsin 53706*

<sup>2</sup>*Department of Physics, University of Wisconsin, Madison, Wisconsin 53706*

<sup>3</sup>*Department of Astronomy, University of Wisconsin, Madison, Wisconsin 53706*

## Abstract

The effects of line-tying on resistive tearing instability in slab geometry is studied within the framework of reduced magnetohydrodynamics (RMHD).[1, 2] It is found that line-tying has a stabilizing effect. The tearing mode is stabilized when the system length  $L$  is shorter than a critical length  $L_c$ , which is independent of the resistivity  $\eta$ . When  $L$  is not too much longer than  $L_c$ , the growthrate  $\gamma$  is proportional to  $\eta$ . When  $L$  is sufficiently long, the tearing mode scaling  $\gamma \sim \eta^{3/5}$  is recovered. The transition from  $\gamma \sim \eta$  to  $\gamma \sim \eta^{3/5}$  occurs at a transition length  $L_t \sim \eta^{-2/5}$ .

---

\*Electronic address: yimin.huang@unh.edu

†Electronic address: zweibel@astro.wisc.edu

## I. INTRODUCTION

The study of the effects of line-tying on magnetohydrodynamic (MHD) instabilities has a long history. In the solar corona, the magnetic field lines of solar coronal loops are deeply anchored (line-tied) to the much denser photosphere. It has long been suggested that because of the stabilizing effect of line-tying, the loops can remain stable for a much longer period of time than expected from MHD instability growth times without line-tying. Raadu was the first to analyze the line-tying stabilization of ideal internal kink mode using the energy principle. [3] Later, more detailed analyses have been done for various resistive [4–7] and ideal MHD instabilities.[8, 9] In recent years, there is a reviving theoretical interest in line-tying, [10–17] partly due to progress from plasma laboratory experiments.[18, 19]

In this paper, we study the effects of line-tying on resistive tearing instability in one of the simplest settings, the slab geometry. The tearing instability in slab geometry is discussed in many textbooks. [20, 21] The equilibrium is a simple current layer where the current is along the  $z$  direction, and the current density only depends on  $x$ . Associated with the current layer is a magnetic field  $B_y$  which changes direction across the current layer. This configuration is ideally stable. With resistivity, the magnetic field can reconnect through the resistive tearing instability. To simplify the analysis, usually a strong guide field perpendicular to the reconnecting field is assumed such that the incompressible approximation may be justified. The configuration we consider here is to place two perfectly conducting end plates perpendicular to the guide field. Therefore, it is the guide field that is line-tied to the end plates. Although this configuration is rather simple, to our knowledge, it has not been studied previously. Velli and Hood have studied the line-tied tearing mode in slab geometry;[5] but in their case, the conducting end plates are perpendicular to the reconnecting field. The model we study here may be regarded as a prototype of more complicated resistive instabilities that arise in coronal heating models based on Parker’s scenario.[22–28]

The rest of the paper is organized as follows. Sec. II sets up the physical model and the governing equations of the system. Sec. III discusses some general properties that can be deduced from the equations without actually solving them. Sec. IV gives a concise description of the numerical methods. The numerical results are presented in Sec. V. We summarize and conclude in Sec. VI.

## II. PHYSICAL MODEL AND GOVERNING EQUATIONS

To simplify the problem, we make the following assumptions: (1) the plasma density is a constant; (2) a strong, constant guide field along the  $z$  axis is present; and (3) the length scales along the guide field are much longer than the length scales in the perpendicular directions. Under these assumptions, the system may be described by the well known reduced MHD (RMHD) equations. [1, 2] In this framework, after proper normalization, the magnetic field and the velocity can be expressed in terms of the flux function  $\psi$  and the stream function  $\phi$  as  $\mathbf{B} = \hat{\mathbf{z}} + \nabla_{\perp}\psi \times \hat{\mathbf{z}}$  and  $\mathbf{u} = \nabla_{\perp}\phi \times \hat{\mathbf{z}}$ . The governing equations are

$$\partial_t \Omega + [\phi, \Omega] = \partial_z J + [\psi, J] + \nu \nabla_{\perp}^2 \Omega, \quad (1)$$

$$\partial_t \psi = \partial_z \phi + [\psi, \phi] + \eta \nabla_{\perp}^2 \psi. \quad (2)$$

Where  $\nu$  and  $\eta$  are the viscosity and the resistivity;  $\nabla_{\perp} \equiv \hat{\mathbf{x}}\partial_x + \hat{\mathbf{y}}\partial_y$  is the perpendicular gradient;  $\Omega = -\nabla_{\perp}^2 \phi$ ,  $J = -\nabla_{\perp}^2 \psi$  are the vorticity and the electric current; and  $[\psi, \phi] \equiv \partial_y \psi \partial_x \phi - \partial_x \psi \partial_y \phi$  is the Poisson bracket. This set of RMHD equations is widely used in studying the coronal heating and current sheet formation problems.[23–34] Two perfectly conducting end plates are placed at  $z = \pm L/2$  to provide the line-tied boundary condition. Although the line-tied condition is an idealization in the sense that the solar photosphere is neither completely rigid nor perfectly conducting, it is a common approximation in solar physics. Strictly speaking, the RMHD ordering  $\partial_z \ll \nabla_{\perp}$  is incompatible with the line-tied boundary condition, due to the presence of a boundary layer near the end plate where  $\partial_z \sim \nabla_{\perp}$ . However, Scheper and Hassam have shown through a boundary layer analysis that RMHD can still be used in the coronal volume, as the boundary layer only appears when the higher order correction to  $B_z$  is calculated. The higher order correction to  $B_z$ , however, is completely decoupled from  $\psi$  and  $\phi$ . [35]

We assume that the equilibrium only depends on  $x$ ; i.e.,  $\mathbf{B} = \hat{\mathbf{z}} - \partial_x \psi \hat{\mathbf{y}} = \hat{\mathbf{z}} + B_y \hat{\mathbf{y}}$ . Consider perturbations of the form  $\tilde{\phi} = \tilde{\phi}(x, z) \exp(ik_y y + \gamma t)$ , and  $\tilde{\psi} = \tilde{\psi}(x, z) \exp(ik_y y + \gamma t)$ . Linearizing the RMHD equations gives

$$\gamma \mathcal{D} \tilde{\phi} = (\partial_z + ik_y B_y) \mathcal{D} \tilde{\psi} - ik_y B_y'' \tilde{\psi} + \nu \mathcal{D}^2 \tilde{\phi}, \quad (3)$$

$$\gamma \tilde{\psi} = (\partial_z + ik_y B_y) \tilde{\phi} + \eta \mathcal{D} \tilde{\psi}. \quad (4)$$

where  $\mathcal{D} \equiv \partial_x^2 - k_y^2$  and the prime denotes  $\partial_x$ . The line-tied boundary condition in the RMHD approximation is simply  $\tilde{\phi} = 0$  at  $z = \pm L/2$ . In this study we will focus on the inertial tearing mode; hereafter the viscosity  $\nu = 0$  is assumed throughout the rest of the paper.

### III. ANALYTICAL CONSIDERATIONS

Although the linearized equations are difficult to solve analytically, some general properties can be readily deduced from analytical considerations. First of all, let us *assume* that there exists a critical length  $L_c$  such that  $\gamma = 0$ . By setting  $\gamma = 0$  and rescaling  $z$  with respect to  $L_c$  (i.e.,  $z \rightarrow L_c z$ ), Eqs. (3) and (4) become

$$-\frac{1}{L_c} \partial_z \mathcal{D} \tilde{\psi} = ik_y B_y \mathcal{D} \tilde{\psi} - ik_y B_y'' \tilde{\psi}, \quad (5)$$

$$-\frac{1}{L_c} \partial_z \tilde{\phi} = ik_y B_y \tilde{\phi} + \eta \mathcal{D} \tilde{\psi}, \quad (6)$$

with the boundary condition  $\tilde{\phi}|_{z=\pm 1/2} = 0$ . Eqs. (5) and (6) may be regarded as an eigenvalue problem with  $1/L_c$  as the eigenvalue. We further notice that by letting  $\tilde{\phi} \rightarrow \eta \tilde{\phi}$ , the parameter  $\eta$  completely drops out of the equations. Therefore, we conclude that the critical length  $L_c$  is independent of  $\eta$ . Some caveats should be mentioned: (1) the existence of  $L_c$  is not guaranteed; (2) the marginal stability may not occur at  $\gamma = 0$ , as pure oscillatory modes are not precluded by the equations. Bearing these caveats in mind, we found numerically that  $L_c$  does exist, and indeed it is independent of  $\eta$ .

Now let us consider an unstable system not too far from marginality, i.e.,  $L \gtrsim L_c$ . If the unstable mode is so slowly growing, we may neglect the inertia term (the left hand side) in Eq. (3). Physically, that means that the system remains force-free throughout the whole domain. Neglecting the inertia term in Eq. (3), and dividing Eq. (4) by  $\eta$ , we come to the following equations for the force-free approximation:

$$0 = (\partial_z + ik_y B_y) \mathcal{D} \tilde{\psi} - ik_y B_y'' \tilde{\psi}, \quad (7)$$

$$(\gamma/\eta) \tilde{\psi} = (\partial_z + ik_y B_y) (\tilde{\phi}/\eta) + \mathcal{D} \tilde{\psi}. \quad (8)$$

It immediately follows that in the force-free approximation, both the growthrate  $\gamma$  and the stream function  $\tilde{\phi}$  scale as  $\eta$ . Since the inertia term  $\sim \gamma \tilde{\phi} \sim \eta^2$ , it is expected that the

force-free approximation works better for smaller  $\eta$ , when everything else remains the same. Recall that in a periodic system, the magnetic field is approximately force-free only in the “outer” region, i.e., far from the resonant surface where  $\mathbf{k} \cdot \mathbf{B} = 0$ . In the inner layer, the resistivity and the inertia are both taken into account. The inner layer thickness  $\delta \sim \eta^{2/5}$ , and the growthrate  $\gamma \sim \eta^{3/5}$  as a result.[36, 37] Naturally, we expect the  $\gamma \sim \eta^{3/5}$  scaling to be recovered if the system is sufficiently long. The operative question is, at what length does this transition occur? We will address this question later.

Finally, we would like to say a few words about the boundary condition. Both Eq. (3) and Eq. (4) are first order differential equations in  $z$ , for  $\tilde{\psi}$  and  $\tilde{\phi}$  respectively. Therefore two boundary conditions are needed. We have two boundary conditions  $\tilde{\phi}|_{z=\pm L/2} = 0$  for  $\tilde{\phi}$ , and none for  $\tilde{\psi}$ . If  $\tilde{\psi}$  is given, then one may integrate Eq. (4) along  $z$  to solve  $\tilde{\phi}$ . In general, the  $\tilde{\phi}$  so obtained can not satisfy both boundary conditions, unless some solubility condition for  $\tilde{\psi}$  is satisfied. Acting on (4) by  $\int_{-L/2}^{L/2} dz e^{ik_y B_y z}$ , after integrating by parts and using the boundary condition on  $\tilde{\phi}$ , we have the solubility condition

$$\gamma \int_{-L/2}^{L/2} dz e^{ik_y B_y z} \tilde{\psi} = \eta \int_{-L/2}^{L/2} dz e^{ik_y B_y z} \mathcal{D} \tilde{\psi}. \quad (9)$$

This solubility condition is not used in the rest of the paper, but we have used it to check the accuracy of the numerical solution.

#### IV. NUMERICAL METHOD

The numerical method we employ may be regarded as a variation of the method proposed by Evstatiev *et al.* in Ref. [14]. In essence, this method is a shooting method in two dimensions. We may rewrite Eqs. (3) (4) in the following form as an evolution equation along  $z$ :

$$\frac{\partial}{\partial z} \begin{bmatrix} \tilde{\psi} \\ \tilde{\phi} \end{bmatrix} = \mathcal{L}_\gamma \begin{bmatrix} \tilde{\psi} \\ \tilde{\phi} \end{bmatrix}, \quad (10)$$

where the operator  $\mathcal{L}_\gamma$  is defined as ( $\nu$  is set to zero)

$$\mathcal{L}_\gamma \equiv \begin{bmatrix} -ik_y \mathcal{D}^{-1}(B_y \mathcal{D} - B_y'') & \gamma \\ \gamma - \eta \mathcal{D} & -ik_y B_y \end{bmatrix}. \quad (11)$$

Starting from an initial condition  $(\tilde{\psi}_0(x), \tilde{\phi}_0(x))$  at  $z = 0$ , we can use Eq. (10) to propagate the initial condition along  $z$ . Formally, the solution may be written as

$$\begin{bmatrix} \tilde{\psi}(x, z) \\ \tilde{\phi}(x, z) \end{bmatrix} = \exp(\mathcal{L}_\gamma z) \begin{bmatrix} \tilde{\psi}_0 \\ \tilde{\phi}_0 \end{bmatrix}. \quad (12)$$

Apparently  $\gamma$  is a eigenvalue if and only if there exists an initial condition at  $z = 0$  such that when propagated to both end caps by Eq. (12), the boundary conditions are satisfied. In the present case, we may consider the linear mapping

$$\mathcal{G}_{\gamma, L} : \begin{bmatrix} \tilde{\psi}_0 \\ \tilde{\phi}_0 \end{bmatrix} \mapsto \begin{bmatrix} \tilde{\phi}(x, z = L/2) \\ \tilde{\phi}(x, z = -L/2) \end{bmatrix}. \quad (13)$$

To simplify the notation, hereafter we will use  $\chi_0$  to denote the initial condition. To satisfy the boundary conditions, we require

$$\sigma_{\gamma, L} \equiv \min_{\chi_0} \frac{\|\mathcal{G}_{\gamma, L} \chi_0\|}{\|\chi_0\|} = 0, \quad (14)$$

where  $\|\cdot\|$  is some suitable norm. Here we use the straightforward generalization of the usual  $L^2$  norm:

$$\|\chi_0\|^2 = \int_{-\infty}^{\infty} \left( |\tilde{\phi}_0|^2 + |\tilde{\psi}_0|^2 \right) dx, \quad (15)$$

$$\|\mathcal{G}_{\gamma, L} \chi_0\|^2 = \int_{-\infty}^{\infty} \left( |\tilde{\phi}(x, L/2)|^2 + |\tilde{\phi}(x, -L/2)|^2 \right) dx. \quad (16)$$

Now if the system length  $L$  is given, one can scan  $\sigma_{\gamma, L}$  over the whole space of complex  $\gamma$ . Those  $\gamma$ 's where  $\sigma_{\gamma, L} = 0$  are the eigenvalues. Alternatively one may fix  $\gamma$  and scan through  $L$  to find out the system lengths for which the given  $\gamma$  is an eigenvalue.

To implement this idea numerically, first we need an accurate discrete approximation for the operator  $\mathcal{L}_\gamma$ . Pseudospectral methods are suitable for the task.[38–40] The numerical integrations for Eqs. (15) and (16) are done with Gaussian quadrature.[41, 42] Since we are dealing with an infinite domain as most textbooks do, we need to map  $(-\infty, \infty)$  smoothly to  $(-1, 1)$  to apply pseudospectral methods. We define the mapping as follows. [43] First

$$x = \frac{c_1 x_1}{\sqrt{1 - x_1^2}} \quad (17)$$

maps  $x_1 \in (-1, 1)$  to  $x \in (-\infty, \infty)$ . Then a second mapping

$$x_2 = (1 - c_3)x_1 + c_3 \frac{2}{\pi} \tan^{-1}(\tan(\pi x_1/2)/c_2) \quad (18)$$

maps  $x_1 \in (-1, 1)$  to  $x_2 \in (-1, 1)$ . This mapping can further concentrate resolution around  $x = 0$  to resolve the resistive layer. The constants  $c_1, c_2, c_3$  are free parameters. A set of  $N$  Legendre-Gauss collocation points[40] are set up in  $x_2$ . The differentiation matrices and Gaussian quadrature weights are first calculated in  $x_2$  with respect to these nodes, then transformed back to  $x$ . In this discrete approximation, the initial condition  $\chi$  is represented by a column vector  $q$ , which consists of  $\tilde{\phi}_0$  and  $\tilde{\psi}_0$  on the collocation points. The operators  $\mathcal{L}_\gamma$  and  $\mathcal{G}_{\gamma,L}$  are represented by matrices  $L_\gamma$  and  $G_{\gamma,L}$ , respectively. The norm is represented by

$$||q||^2 = q^\dagger W q, \quad (19)$$

where  $\dagger$  denotes the conjugate transpose and  $W$  is a real diagonal matrix from the Gaussian quadrature. We have to find

$$\sigma_{\gamma,L} = \min_q \frac{(q^\dagger G_{\gamma,L}^\dagger W G_{\gamma,L} q)^{1/2}}{(q^\dagger W q)^{1/2}} \quad (20)$$

and the corresponding  $q$  that gives the minimum. Let  $W = M^\dagger M$  and  $s = Mq$ . Then

$$\sigma_{\gamma,L} = \min_s \frac{(s^\dagger M^{-1\dagger} G_{\gamma,L}^\dagger M^\dagger M G_{\gamma,L} M^{-1} s)^{1/2}}{(s^\dagger s)^{1/2}}. \quad (21)$$

Now we calculate the singular value decomposition (SVD) [42]  $M G_{\gamma,L} M^{-1} = U S V^\dagger$ , where  $U$  and  $V$  are unitary matrices of left and right singular vectors, and  $S$  is a real nonnegative diagonal matrix of singular values. Then  $\sigma_{\gamma,L}$  is the smallest singular value, and  $q = M^{-1}s$ , where  $s$  is the right singular vector (a column of  $V$ ) corresponding to the smallest singular value. The eigenfunction can be reconstructed by propagating  $q$  along  $z$  by  $\exp(\mathcal{L}_\gamma z)$ .

Fig. 1 shows  $\log(\sigma_{\gamma,L})$  within a domain of complex  $\gamma$  for the case  $\eta = 10^{-4}$ ,  $L = 1000$ . Those  $\gamma$ 's where  $\sigma_{\gamma,L}$  goes to zero are eigenvalues. In this particular case, we found six eigenvalues within the domain, all on the real axis. It is rather computationally expensive to scan through a complex domain. Fortunately, we found that the most unstable mode always has a real eigenvalue. Therefore we only scan through the real axis for most of our calculation.

Here we briefly compare our method with the method of Evstatiev *et al.* in Ref. [14]. These authors let  $\partial_z \rightarrow \lambda$  (they use  $ik$  instead of  $\lambda$ ) in Eq. (10) then solve it as an auxiliary eigenvalue problem. Let  $\lambda_i e_i = \mathcal{L}_\gamma e_i$ , where  $\lambda_i$  is the eigenvalue and  $e_i$  the eigenfunction of  $\mathcal{L}_\gamma$ . The general solution is written as  $\chi = \sum_{i=1}^n a_i e^{\lambda_i z} e_i$  (truncated to a finite number of  $n$

modes), which satisfies Eq. (10). To impose the boundary conditions, they consider

$$\bar{\sigma}_{\gamma,L} = \min_{a_i} \frac{\left(\sum_{j=1}^m |\chi_j|^2\right)^{1/2}}{\left(\sum_{i=1}^n |a_i|^2\right)^{1/2}}, \quad (22)$$

where we use  $\chi_j$  to symbolically denote the value of the solution (in the present case, the  $\tilde{\phi}$  part only) on a set of  $m$  points (which can be arbitrarily chosen, with  $m \geq n$ ) on the end plates. Scanning through  $\gamma$  for a given  $L$  (or through  $L$  for a given  $\gamma$ ), the local minimum of  $\bar{\sigma}_{\gamma,L}$  corresponds to an eigenmode of the original eigenvalue problem. Now it is clear that the two approaches are rather similar, and the differences are only minor details. If the eigenmodes of  $\mathcal{L}_\gamma$  form a complete basis, projecting onto the eigenbasis is a convenient and efficient way of finding  $\exp(\mathcal{L}_\gamma z)$ . Explicitly, if  $\chi_0 = \sum_i a_i e_i$ , then  $\exp(\mathcal{L}_\gamma z) \chi_0 = \sum_i a_i e^{\lambda_i z} e_i$ . Instead of representing  $\chi_0$  by its value on collocation points, one may use the expansion coefficients  $\{a_i\}$ . The linear mapping  $\mathcal{G}_{\gamma,L}$ , the norm  $\|\cdot\|$ , and  $\sigma_{\gamma,L}$  can be similarly defined in terms of  $\{a_i\}$ . Formulated in this way, our approach is nearly identical to theirs. The only real difference between the two is that we use  $\sigma_{\gamma,L}$  instead of  $\bar{\sigma}_{\gamma,L}$ . It is worth pointing out, however, that even if the eigenmodes of  $\mathcal{L}_\gamma$  are not complete,  $\exp(\mathcal{L}_\gamma z)$  may still exist.<sup>1</sup> Therefore our method does *not* rely on the existence of a complete eigenbasis.

The advantage of  $\sigma_{\gamma,L}$  is that it has a precise, analytical definition, Eq. (14); and Eq. (20) is merely a numerical approximation to it. This allows us an easier way to check convergence — if the numerical solution is fully converged,  $\sigma_{\gamma,L}$  should be independent of the resolution and the mapping parameters. On the other hand, the definition of  $\bar{\sigma}_{\gamma,L}$  depends on the points chosen to enforce the boundary condition, the set of eigenmodes  $\{e_i\}_{i=1}^n$  for expansion, as well as the normalization of the eigenmodes. Fig. 2 shows a case of our convergence test with respect to the resolution, for  $N = 50, 75, 100$ . The  $N = 50$  calculation gives  $\gamma \simeq 1.301 \times 10^{-4}$ , while the other two calculations give  $\gamma \simeq 1.299 \times 10^{-4}$ . Note that the curves from  $N = 75$  and  $N = 100$  calculations are almost identical, indicating convergence. For  $N > 100$  calculations, the results are virtually indistinguishable from the  $N = 100$  curve. Fig. 3 shows the eigenfunction  $\tilde{\psi}$  from the same calculations. Although the relative error in the eigenvalue from the  $N = 50$  calculation is only about 0.2%, the eigenfunction

---

<sup>1</sup> As a simple example, consider  $A = [3, -2; 2, -1]$ , which has only one eigenvalue 1 as a double root and only one corresponding eigenvector (1, 1); therefore  $A$  does not have a complete eigenbasis. However,  $\exp(Az) = e^z [1 + 2z, -2z; 2z, 1 - 2z]$  is well defined.



is clearly not accurate. The  $N = 75$  result is much better, but there are still wiggles on the imaginary part. The  $N = 100$  calculation gives a fully converged eigenfunction. This once again demonstrates that an accurate eigenfunction is much more difficult to obtain than the eigenvalue. It took significant effort to make sure all the numerical results presented in this work are fully converged.

## V. RESULTS

We use the Harris sheet  $B_y = b \tanh(x)$ ,  $b = 0.1$ , as the equilibrium. The wavenumber  $k_y = 0.5$  is used for most of the calculations. The dependence on  $k_y$  will be addressed later.

### A. Periodic System

The periodic system is usually solved for the case  $k_z = 0$ , but the analysis can be easily generalized to  $k_z \neq 0$  cases. In the so-called constant  $\psi$  approximation (i.e.  $\tilde{\psi}$  is approximately constant within the resistive layer), the growthrate  $\gamma$  is proportional to  $\eta^{3/5}$ . [36, 37] Fig. 4 shows the growthrate  $\gamma$  divided by  $\eta^{3/5}$  as a function of  $k_z$ , for different  $\eta$ . In the asymptotic limit  $\eta \rightarrow 0$ , all curves should lie on top of each other. Some interesting features may be readily observed: (1) Except for the case  $\eta = 10^{-4}$ ,  $k_z = 0$  is not the peak of the growthrate. As we will see, this has an interesting consequence in line-tied solutions. (2) The  $\gamma \sim \eta^{3/5}$  scaling works better around  $k_z = 0$ . This may be due to the fact that it is easier to satisfy the constant  $\psi$  approximation there. However, we expect that as long as  $\eta$  is sufficiently small, eventually the constant  $\psi$  approximation will work for all  $k_z$ .

At first sight, it may seem counter-intuitive that  $k_z = 0$  is a local minimum of  $\gamma$ . In the tearing mode analysis  $\gamma$  is determined by  $\Delta'$  and  $(\mathbf{k} \cdot \mathbf{B})'$  at the resonant surface. For the Harris sheet profile  $\Delta'$  may be difficult to calculate analytically when  $k_z \neq 0$ . However, for a similar piecewise linear profile, i.e.  $B_y = bx$  when  $|x| \leq 1$  and  $B_y = bx/|x|$  when  $|x| \geq 1$ , an analytic  $\Delta'$  can be found. It may be shown that in this case  $k_z = 0$  is also a local minimum. In fact,  $\Delta'$  diverges as  $k_z \rightarrow \pm k_y b$ . This pathological behavior may be due to the abrupt turning of  $B_y$  at  $x = \pm 1$ , which is unphysical. However, the result from this simple system suggests that it may be generic, or at least rather unsurprising, that  $k_z = 0$  is the local minimum for the system we consider here.

## B. Line-tied System

The growthrate  $\gamma$  of the fastest growing mode as a function of  $L$  for various  $\eta$  is summarized in Fig. 5. In the plot we normalized  $\gamma$  with respect to  $\eta$ . As discussed in Sec. III, we expect the critical length  $L_c$  to be independent of  $\eta$ , and  $\gamma$  to be proportional to  $\eta$  near marginality. Both are borne out by the numerical calculations. It is found that  $L_c = 115.09$  for all  $\eta$ , and the  $\gamma/\eta$  versus  $L$  curves all coincide with the prediction from the force-free approximation. As  $L$  becomes longer, the curve starts to deviate from the force-free approximation. The deviation occurs earlier the larger  $\eta$  is. This is also what we expect in Sec. III. The horizontal bars denote the range determined by the periodic  $\gamma$  at  $k_z = 0$  and the maximum periodic  $\gamma$  (see Fig. 4). We observe that as the growthrate peels away from the force-free approximation, it first goes beyond the periodic  $\gamma$  at  $k_z = 0$ , and eventually levels off at (but never exceeds) the maximum periodic  $\gamma$ . Therefore the force-free approximation and the maximum periodic growthrate may be regarded as two asymptotes of the line-tied growthrate. We are not able to achieve fully converged results as the  $\eta = 10^{-6}$  and  $10^{-7}$  cases approach their periodic limits. However, based on the observation for larger  $\eta$  cases, it is fairly safe to say that the two-asymptote scheme may be generally applicable.

Fig. 6 and Fig. 7 show the eigenfunctions  $|\tilde{\phi}|$  and  $|\tilde{\psi}|$  for various  $L$ , with  $\eta = 10^{-5}$ . The eigenfunction is normalized such that  $\tilde{\psi}(0,0) = 1$ . The eigenfunction is very smooth at the critical length  $L_c = 115.09$ . As  $L$  becomes longer, the internal layer at  $x = 0$  become steeper and steeper. Up to  $L = 1000$ , the eigenfunction still largely covers the whole length along  $z$ . At  $L = 1500$  and  $2000$ , the eigenfunction becomes localized to the midplane. This localization is more pronounced in  $\tilde{\psi}$ . At  $L = 3500$ , the growthrate is greater than the periodic one at  $k_z = 0$ . The internal layer “splits” into two, and there are wiggles along the  $z$  direction. This is due to the peculiar two-bump structure in the dispersion relation of the periodic system (Fig. 4). In the periodic system,  $\gamma > \gamma|_{k_z=0}$  corresponds to four nonzero  $k_z$ ’s, therefore we expect the line-tied mode to be dominated by  $k_z \neq 0$  behavior. The four periodic modes have resonant surfaces at four different locations. The four resonant surfaces form two pairs, one in  $x > 0$  and the other in  $x < 0$ . These two pairs of resonant surfaces roughly correspond to the two parts of the split internal layer. From the discussion in Ref. [14–16], we expect an expansion from four eigenmodes of  $\mathcal{L}_\gamma$  to be a good approximation when the two resonant surfaces within each pair become sufficiently close to each other.

However, it is found that for this to occur one would have to go to an enormously large  $L$ , and we have trouble achieving full convergence in this regime.

As a comparison, Fig. 8 shows the eigenfunction  $|\tilde{\phi}|$  with the same parameters as Fig. 6, but in the force-free approximation. The force-free approximation for  $L = 400$  is almost identical with the real solution. Even at  $L = 1000$ , the force-free solution is still not too far from the real one. At  $L = 1500$  and beyond, the difference between the two is significant. The same conclusion can be drawn from Fig. 5, where the force-free dispersion relation is good for up to  $L = 1000$ , then it starts to depart from the real one. We also observe that the internal layer of the force-free eigenfunction keep getting steeper as  $L$  increases. Fig. 9 shows the midplane cut of  $\text{Im}(\tilde{\phi})$  for various  $L$ , and Fig. 10 shows its force-free counterpart. Also shown in both figures is the  $k_z = 0$  periodic eigenmode with the inertia term included, for reference. Notice that in periodic systems, the inertia term has to be included to resolve the inner layer,[36, 37] while in line-tied configurations the inner layer can be resolved with the help of the boundary condition (no  $\mathbf{k} \cdot \mathbf{B} = 0$  singularity) alone. Following the convention of Ref. [16], the internal layer width of the force-free approximation is called the “geometric” width, and that of the periodic eigenmode is called the “tearing” width. At  $L = 1500$ , the geometric width is approximately the same as the tearing width, and this is exactly when the force-free approximation is about to fail.

Therefore, we come to the conclusion that the transition from the resistive scaling  $\gamma \sim \eta$  to the tearing scaling  $\gamma \sim \eta^{3/5}$  occurs when the inertia term is no longer negligible, or equivalently, when the tearing width is comparable to the geometric width. This prompts us to do a scaling analysis similar to the one of Ref. [16]. Assuming the constant  $\psi$  approximation, and letting  $\delta$  be the thickness of the internal layer, we have  $\mathcal{D}\tilde{\phi} \sim \tilde{\phi}/\delta^2$ ,  $\mathcal{D}\tilde{\psi} \sim \tilde{\psi}\Delta'/\delta$ , and  $B_y \sim B'_y\delta$  within the layer, where  $\Delta'$  is the jump of  $\tilde{\psi}'$  across the layer divided by  $\tilde{\psi}$ . [36, 37] For the periodic case, we have  $\gamma\mathcal{D}\tilde{\phi} \sim k_y B_y \mathcal{D}\tilde{\psi}$  and  $\gamma\tilde{\psi} \sim k_y B_y \tilde{\phi} \sim \eta\mathcal{D}\tilde{\psi}$  within the layer. That is

$$\gamma\tilde{\phi}/\delta^2 \sim k_y B'_y \Delta' \tilde{\psi}, \quad (23)$$

$$\gamma\tilde{\psi} \sim k_y B'_y \delta \tilde{\phi} \sim \eta\tilde{\psi}\Delta'/\delta. \quad (24)$$

From that, we find the tearing growthrate

$$\gamma_{tearing} \sim (k_y B'_y)^{2/5} \Delta'^{4/5} \eta^{3/5}, \quad (25)$$

and the tearing width

$$\delta_{tearing} \sim \eta^{2/5} \Delta'^{1/5} (k_y B'_y)^{-2/5}. \quad (26)$$

For the line-tied case with the force-free approximation, we may assume  $\partial_z \sim 1/L$  since the eigenfunction spreads over the entire length (Fig. 8). Within the internal layer, we have  $\partial_z \sim k_y B_y$ ; i.e., the geometric width

$$\delta_{geometric} \sim 1/k_y B'_y L. \quad (27)$$

From the induction equation, we have

$$\gamma_{force-free} \sim \eta \Delta' / \delta \sim \eta k_y B'_y L \Delta'. \quad (28)$$

Also, we may estimate  $\tilde{\phi}$  from  $\gamma \tilde{\psi} \sim k_y B'_y \delta \tilde{\phi}$  as

$$\tilde{\phi} \sim \eta k_y B'_y L^2 \Delta' \tilde{\psi}. \quad (29)$$

The force-free approximation is self-consistent if  $\gamma \mathcal{D} \tilde{\phi} \ll \partial_z \mathcal{D} \tilde{\psi}$ ; i.e.,  $\gamma \tilde{\phi} / \delta^2 \ll \tilde{\psi} \Delta' / \delta L$ . Using Eqs. (27), (28), and (29), the self-consistency condition can be written as

$$L \ll L_t \sim \eta^{-2/5} \Delta'^{-1/5} (k_y B'_y)^{-3/5}, \quad (30)$$

where  $L_t$  is the transition length from resistive scaling to tearing scaling. The same condition can be obtained if we require  $\delta_{tearing} \ll \delta_{geometric}$ .

The scaling analysis predicts that the transition length  $L_t \sim \eta^{-2/5}$ . Also we know that as  $L$  becomes large,  $\gamma \sim \eta^{3/5}$ . This motivates us to rescale Fig. 5 in the following way. We plot  $\gamma / \eta^{3/5}$  versus  $(L - L_c) \eta^{2/5}$ . Normalizing  $\gamma$  by  $\eta^{3/5}$  brings the asymptotic regime to the same level, while multiplying  $(L - L_c)$  by  $\eta^{2/5}$  brings the transition length to the same place. The result is shown in Fig. 11. Clearly those curves for different  $\eta$  become close to each other, especially those with smaller  $\eta$  are almost identical. Therefore the numerical results agree with the  $L_t \sim \eta^{-2/5}$  prediction. The analysis also predicts  $\gamma_{force-free} \sim \eta k_y B'_y L \Delta'$ . We can see from Fig 5 that the force-free dispersion relation is very close to a straight line. That suggests that we may associate the slope with  $\gamma_{force-free} / \eta L \sim k_y B'_y \Delta'$ . For the Harris sheet profile,  $\Delta' = 2(1/k_y - k_y)$ . To test the conjecture we have to find the slope for different  $k_y$ . The slope and the critical length for different  $k_y$  are summarized in Table II. We found that  $L_c$  only weakly depends on  $k_y$ . Fitting the slope with  $\text{const} \times k_y \Delta' B'_y$  gives slope  $\simeq 0.0159 k_y \Delta' B'_y$ . This turns out to be an excellent fit, as shown in Fig. 12.

$k_y$	$L_c$	Slope	$k_y \Delta' B'_y$
0.3	112.85	0.0288	0.182
0.4	111.50	0.0266	0.168
0.5	115.09	0.0239	0.150
0.6	123.86	0.0204	0.128
0.7	141.09	0.0162	0.102

Table II: The critical length  $L_c$  and the slope of the force-free dispersion relation  $\gamma/\eta$  versus  $L$  for different  $k_y$ . Also shown is the corresponding  $k_y \Delta' B'_y$ . The scaling analysis suggests that slope  $\sim k_y \Delta' B'_y$ .

## VI. SUMMARY AND DISCUSSION

In this work, we study the effects of line-tying on the resistive tearing instability in great detail. We found that line-tying has a stabilizing effect, and instability occurs only when the system length is greater than a critical length  $L_c$ , which is independent of the resistivity  $\eta$ . When the system length is not too long, the plasma inertia is negligible. In other words, the plasma is approximately force-free throughout the whole domain. In this regime, the growthrate  $\gamma$  is proportional to  $\eta$  and the internal layer of the unstable mode is much wider compared to the periodic mode. The tearing mode scaling  $\gamma \sim \eta^{3/5}$  is recovered when the system becomes sufficiently long. The transition from  $\gamma \sim \eta$  to  $\gamma \sim \eta^{3/5}$  occurs when the plasma inertia is no longer negligible within the resistive layer; this is also when the “geometric” width becomes comparable to the “tearing” width. The transition length  $L_t$  scales like  $\eta^{-2/5}$ .

Physically it is not hard to understand why the growthrate in the force-free approximation is proportional to  $\eta$ . In the original system, there are two time scales, the Alfvénic time scale and the resistive time scale; and the tearing mode grows at a hybrid time scale of the two. If the inertia is neglected completely, the resistive time scale is the only one left; therefore the mode can only grow on the resistive time scale. However, neglecting the inertia in the entire domain is possible only in a line-tied system, as the line-tied boundary conditions serve as a means of resolving the singularity at the rational surface. In a periodic system, the inertia

term always comes into play in the vicinity of the rational surface.

The periodic growthrate and the growthrate from the force-free approximation may be regarded as two asymptotes of the line-tied growthrate. The force-free growthrate  $\gamma_{force-free}$  is approximately linear with respect to  $L$  and the slope is found to be related to  $\Delta'$ . To a very good approximation  $\gamma_{force-free} \simeq 0.0159k_y\Delta'B'_y\eta(L - L_c)$ , where  $B'_y$  is evaluated at  $x = 0$ . Unfortunately, we do not have a good way to estimate the critical length  $L_c$ .

To a large extent, our findings are in agreement with the earlier study by Delzanno and Finn in cylindrical geometry.[15] One major discrepancy is that we found  $L_t \sim \eta^{-2/5}$  while they reported  $L_t \sim \eta^{-1/4.2} \sim \eta^{-0.24}$  (They actually consider the crossover resistivity  $\eta_{cross}$  for a given  $L$ , and find  $\eta_{cross} \sim L^{-4.2}$ ; but this is just a matter of which variable is held fixed). A possible explanation for the discrepancy is that they use a fairly large viscosity, which remains unchanged when other parameters are varied. We have not studied the effect of viscosity in great detail. Some preliminary results indicate that viscosity does have a significant effect, and  $L_t \sim \eta^{-2/5}$  scaling is no longer valid when a large viscosity is added.

We conclude with a brief discussion of our findings in the context of solar corona. The solar corona is very highly conducting, and the aspect ratios of observed coronal loops are 10 – 100, far smaller than necessary for growthrates in the tearing regime. Therefore it is likely the resistive instability will operate in the  $\gamma \sim \eta$  regime. An immediate question is that, since the resistive time scale is so long in the solar corona, is the resistive instability relevant at all? We do not have a clear answer as yet. It is quite clear that our model is highly idealized and has some obvious shortcomings. An immediate concern is that footpoint drivers are not included in our analysis; therefore the equilibrium profile will decay on a resistive time scale  $\tau_\eta$ . Our analysis implicitly assumes either that  $\gamma \gg 1/\tau_\eta$ , such that the resistive decay may be neglected, or that the equilibrium is maintained by some external current drive, as in laboratory devices. In the solar corona the electric current is driven by footpoint motions, and the assumption is clearly inadequate when  $L_c < L \ll L_t$ , as the growthrate  $\gamma$  is either comparable to or even smaller than  $1/\tau_\eta$ . A remedy to this problem would be adding a footpoint driver to the system to maintain the equilibrium. This will add an overall background flow to the equilibrium and potentially have some effect on the stability, especially when the system is close to marginal stability. Detailed analysis is left to a future study. Furthermore, the rigid wall boundary condition, which we take for simplicity, may be too restrictive as argued by some workers. This is especially true when considering

modes with  $\gamma \sim \eta$ , as the photosphere may be able to respond during the slow time scale of growth. A proper treatment requires some detailed knowledge of the photosphere interior. [7, 44–46] In light of these shortcomings, our findings certainly need further scrutiny when applied to the solar corona.

As a final remark, the nonlinear evolution of the mode has to be studied. Indeed, even in the classical tearing mode theory without line-tying, the unstable mode evolves into the nonlinear regime very quickly.[47] Our preliminary study indicates that thin current filaments can be created within the original current layer as the mode evolves nonlinearly. Therefore the role resistive instabilities play in current sheet thinning cannot be overlooked. Another interesting point is that, since the stability criterion does not depend on the resistivity but the growthrate does, the solar corona may appear to be quiescent but already be in an unstable configuration. The slow growthrate of the resistive instability allows the corona to be driven well beyond the critical point, therefore more free energy could be stored. Yet the resistive instability, however slow it may be, also provides a means for the corona to tap into the free energy in an otherwise ideally stable configuration. The multiple roles the resistive instability may play here leave much to ponder about. We hope to address some of these issues in the future.

### Acknowledgments

It is a pleasure to acknowledge beneficial discussions with Dr. G. L. Delzanno, Dr. E. G. Evstatiev, and Dr. J. M. Finn about their numerical methods and the physics of line-tying. Yi-Min Huang would like to thank Daniel Lecoanet and Nick Murphy for inspirations. Yi-Min Huang also thanks Prof. A. Bhattacharjee for the support to present this work in the annual meeting of American Physical Society, Division of Plasma Physics. The authors gratefully acknowledge the insightful comments from the referee. This research is supported by the National Science Foundation, Grant No. PHY-0215581 (PFC: Center for Magnetic Self-Organization in Laboratory and Astrophysical Plasmas).

- 
- [1] B. B. Kadomtsev and O. P. Pogutse, Sov. Phys. JETP **38**, 283 (1974).
  - [2] H. R. Strauss, Phys. Fluids **19**, 134 (1976).

- [3] M. A. Raadu, Solar Physics **22**, 425 (1972).
- [4] M. Velli and A. W. Hood, Solar Physics **106**, 353 (1986).
- [5] M. Velli and A. W. Hood, Solar Physics **119**, 107 (1989).
- [6] M. Velli, A. W. Hood, and G. Einaudi, Astrophys. J. **350**, 419 (1990).
- [7] A. B. Hassam, Astrophys. J. **348**, 778 (1990).
- [8] M. Velli, A. W. Hood, and G. Einaudi, Astrophys. J. **350**, 428 (1990).
- [9] E. G. Zweibel and D. L. Bruhwiler, Astrophys. J. **399**, 318 (1992).
- [10] C. C. Hegna, Phys. Plasmas **11**, 4230 (2004).
- [11] D. D. Ryutov, R. H. Cohen, and L. D. Pearlstein, Phys. Plasmas **11**, 4740 (2004).
- [12] D. D. Ryutov, I. Furno, T. P. Intrator, A. S., and T. Madziwa-Nussinov, Phys. Plasmas **13**, 032105 (2006).
- [13] Y.-M. Huang, E. G. Zweibel, and C. R. Sovinec, Phys. Plasmas **13**, 092102 (2006).
- [14] E. G. Evstatiev, G. L. Delzanno, and J. M. Finn, Phys. Plasmas **13**, 072902 (2006).
- [15] G. L. Delzanno, E. G. Evstatiev, and J. M. Finn, Phys. Plasmas **14**, 072902 (2007).
- [16] G. L. Delzanno and J. M. Finn, Phys. Plasmas **15**, 032904 (2008).
- [17] V. A. Svidzinski, V. V. Mirnov, and H. Li, Phys. Plasmas **15**, 092106 (2008).
- [18] W. F. Bergerson, C. B. Forest, G. Fiksel, D. A. Hannum, R. Kendrick, J. S. Sarff, and S. Stambler, Phys. Rev. Lett. **96**, 015004 (2006).
- [19] X. Sun, T. P. Intrator, L. Dorf, I. Furno, and G. Lapenta, Phys. Rev. Lett. **100**, 205004 (2008).
- [20] R. J. Goldston and P. H. Rutherford, *Introduction to Plasma Physics* (Institute of Physics Publishing, Philadelphia, 1995).
- [21] P. A. Sturrock, *Plasma Physics: an Introduction to the theory of Astrophysical, Geophysical, and Laboratory Plasmas* (Cambridge University Press, 1994).
- [22] E. N. Parker, Astrophys. J. **174**, 499 (1972).
- [23] P. Dmitruk, D. O. Gómez, and E. E. DeLuca, Astrophys. J. **505**, 974 (1998).
- [24] P. Dmitruk and D. O. Gómez, Astrophys. J. **527**, L63 (1999).
- [25] P. Dmitruk, D. O. Gómez, and W. H. Matthaeus, Phys. Plasmas **10**, 3584 (2003).
- [26] A. F. Rappazzo, R. B. Dahlburg, G. Einaudi, and M. Velli, Advances in Space Research **37**, 1335 (2006).
- [27] A. F. Rappazzo, M. Velli, G. Einaudi, and R. B. Dahlburg, Astrophys. J. **657**, L47 (2007).



- [28] A. F. Rappazzo, M. Velli, G. Einaudi, and R. B. Dahlburg, *Astrophys. J.* **677**, 1348 (2008).
- [29] D. W. Longcope and R. N. Sudan, *Astrophys. J.* **384**, 305 (1992).
- [30] D. W. Longcope and R. N. Sudan, *Phys. Rev. Lett.* **68**, 1706 (1992).
- [31] D. W. Longcope and R. N. Sudan, *Phys Fluids B-Plasma Phys.* **4**, 2277 (1992).
- [32] D. W. Longcope and H. R. Strauss, *Astrophys. J.* **437**, 851 (1994).
- [33] D. W. Longcope and R. N. Sudan, *Astrophys. J.* **437**, 491 (1994).
- [34] C. S. Ng and A. Bhattacharjee, *Phys. Plasmas* **5**, 4028 (1998).
- [35] R. A. Scheper and A. B. Hassam, *Astrophys. J.* **511**, 976 (1999).
- [36] H. P. Furth, J. Killeen, and M. N. Rosenbluth, *Phys. Fluids* **6**, 459 (1963).
- [37] R. B. White, *Rev. Mod. Phys.* **58**, 183 (1986).
- [38] L. N. Trefethen, *Spectral Methods in Matlab* (SIAM Philadelphia, 2000).
- [39] W. J. A. C. and S. C. Reddy, *ACM Transactions on Mathematical Software* **26**, 465 (2000).
- [40] B. Fornberg, *A Practical Guide to Pseudospectral Methods* (Cambridge University Press, 1995).
- [41] W. H. Press, S. A. Teukolsky, W. T. Vetterling, and B. P. Flannery, *Numerical Recipes in C++: The Art of Scientific Computing* (Cambridge University Press, 2002), 2nd ed.
- [42] L. N. Trefethen and D. Bau, III, *Numerical Linear Algebra* (SIAM Philadelphia, 1997).
- [43] J. P. Boyd, *Chebyshev and Fourier Spectral Methods* (Dover Publications, Inc., 2001), 2nd ed.
- [44] A. W. Hood, *Solar Physics* **105**, 307 (1986).
- [45] R. A. M. van der Linden, A. W. Hood, and J. P. Goedbloed, *Solar Physics* **154**, 69 (1994).
- [46] E. G. Zweibel, *Geophys. Astrophys. Fluid Dyn.* **32**, 317 (1985).
- [47] P. H. Rutherford, *Phys. Fluids* **16**, 1903 (1973).

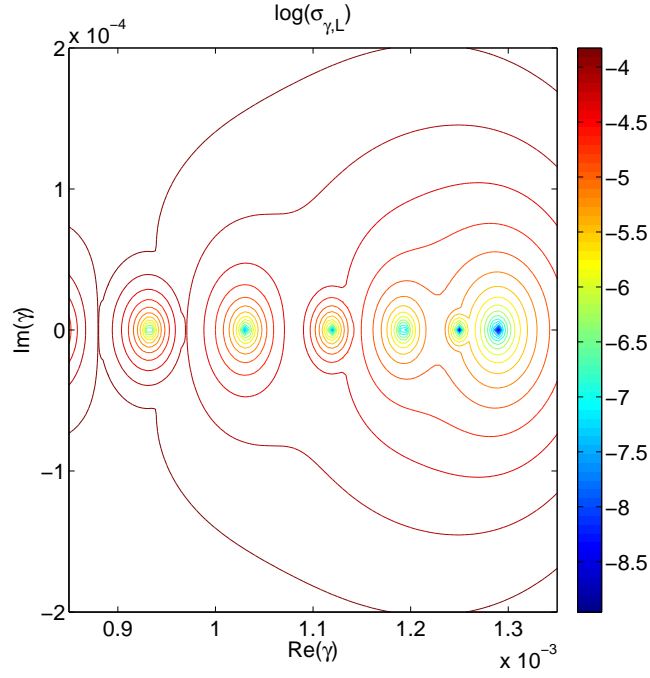


Figure 1: (Color online)  $\log(\sigma_{\gamma,L})$  in a domain of complex  $\gamma$ .  $\eta = 10^{-4}$  and  $L = 1000$ . Those  $\gamma$ 's where  $\sigma_{\gamma,L}$  goes to zero are eigenvalues. Here we found six eigenvalues within this domain. All of them are on the real axis.

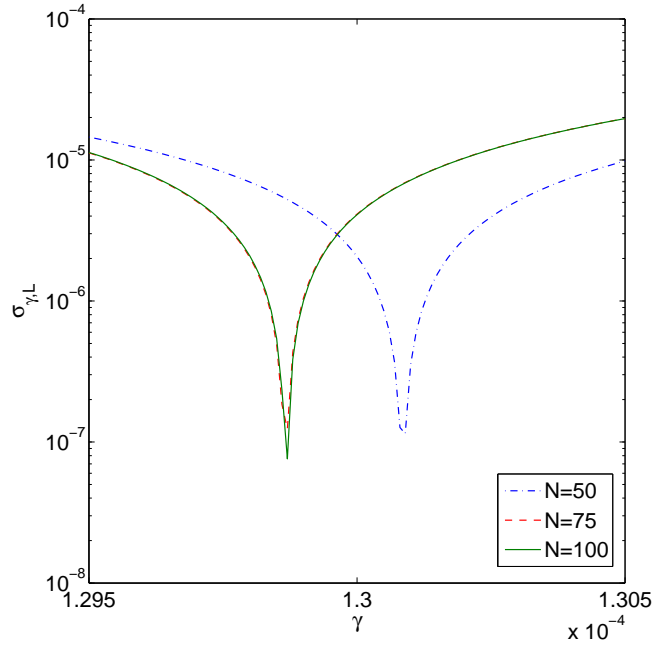


Figure 2: (Color online) Convergence test for the case  $\eta = 3 \times 10^{-6}$ ,  $L = 2000$ . The mapping parameters are  $c_1 = 2$ ,  $c_2 = 0.1$ ,  $c_3 = 0.9$ . The  $N = 50$  calculation gives  $\gamma \simeq 1.301 \times 10^{-4}$ , while the other two calculations give  $\gamma \simeq 1.299 \times 10^{-4}$ . Note that the curves from  $N = 75$  and  $N = 100$  calculations are almost identical, that indicates convergence. For  $N > 100$  calculations, the results are virtually indistinguishable from the  $N = 100$  curve.

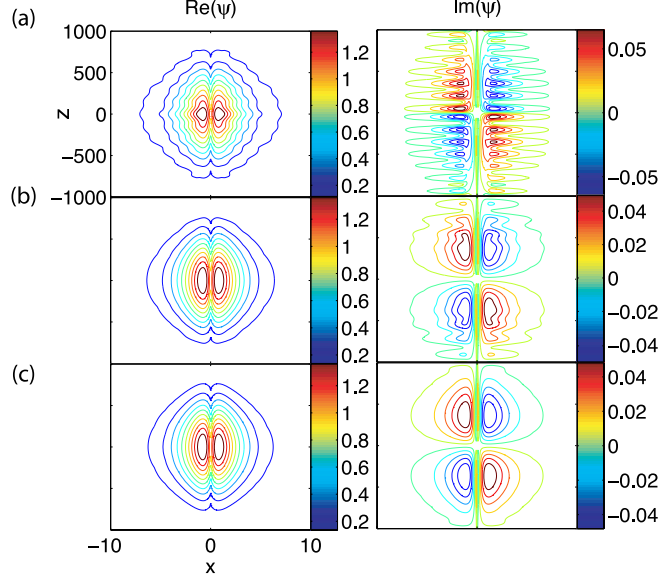


Figure 3: (Color online) The real and imaginary parts of eigenfunctions  $\tilde{\psi}$  from the convergence test shown in Fig. 2. (a)  $N=50$ , (b)  $N=75$ , (c)  $N=100$ . Note that although the relative error on eigenvalue from  $N = 50$  calculation is only about 0.2%, the eigenfunction is clearly not accurate. The  $N = 75$  result is much better, but there are still wiggles on the imaginary part. The  $N = 100$  calculation gives a fully converged eigenfunction.

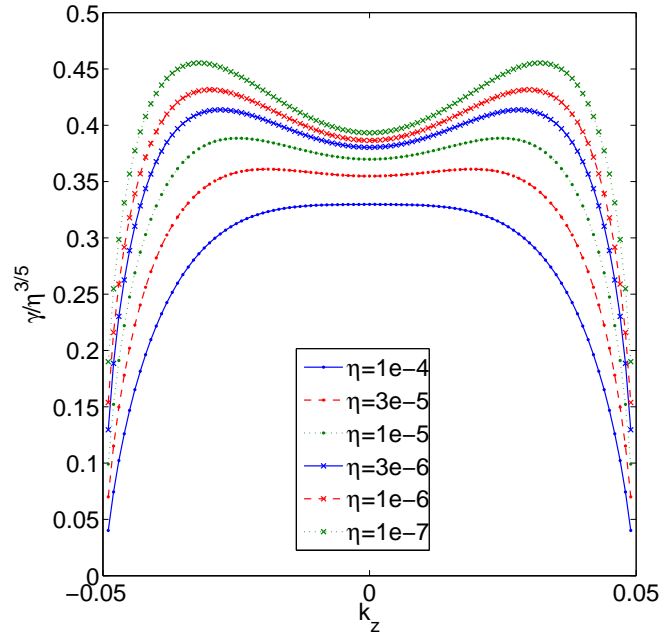


Figure 4: (Color online)  $\gamma/\eta^{3/5}$  as a function of  $k_z$ , for periodic systems.

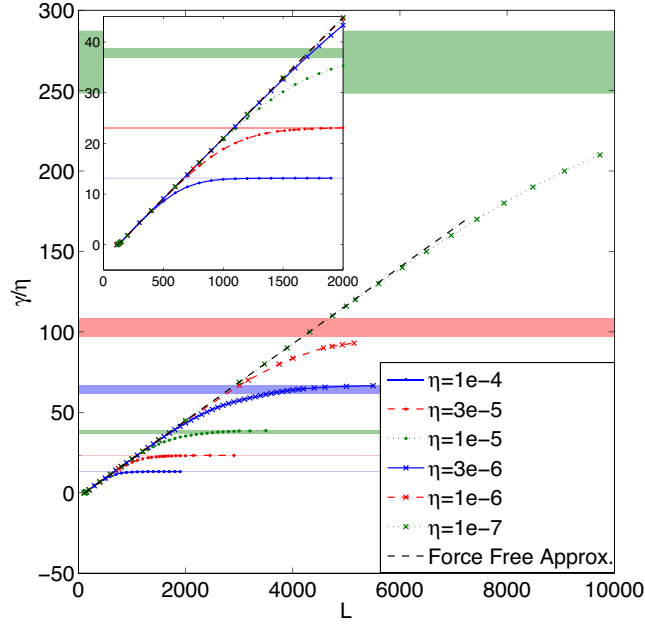


Figure 5: (Color online)  $\gamma/\eta$  as a function of  $L$ , for various  $\eta$ . The horizontal bars denote the range determined by the periodic  $\gamma$  at  $k_z = 0$  and the the maximum periodic  $\gamma$  (see Fig. 4). The dashed line is the prediction from the force-free approximation. Inset: the expanded view of the lower left corner.

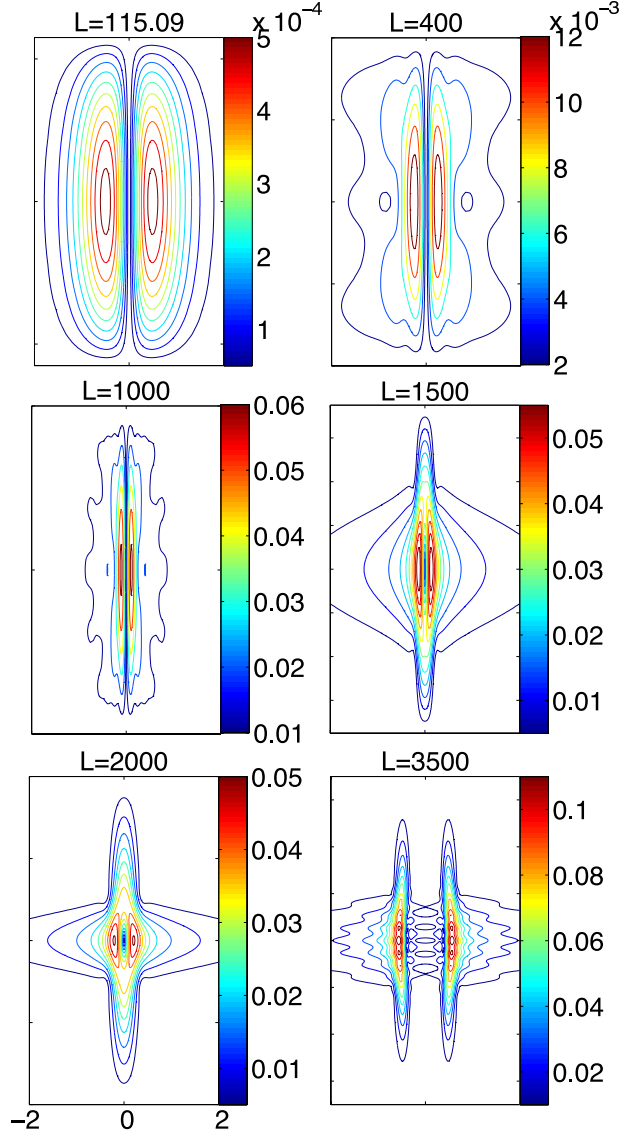


Figure 6: (Color online) The eigenfunction  $|\tilde{\phi}|$  for various  $L$ .  $\eta = 10^{-5}$ .

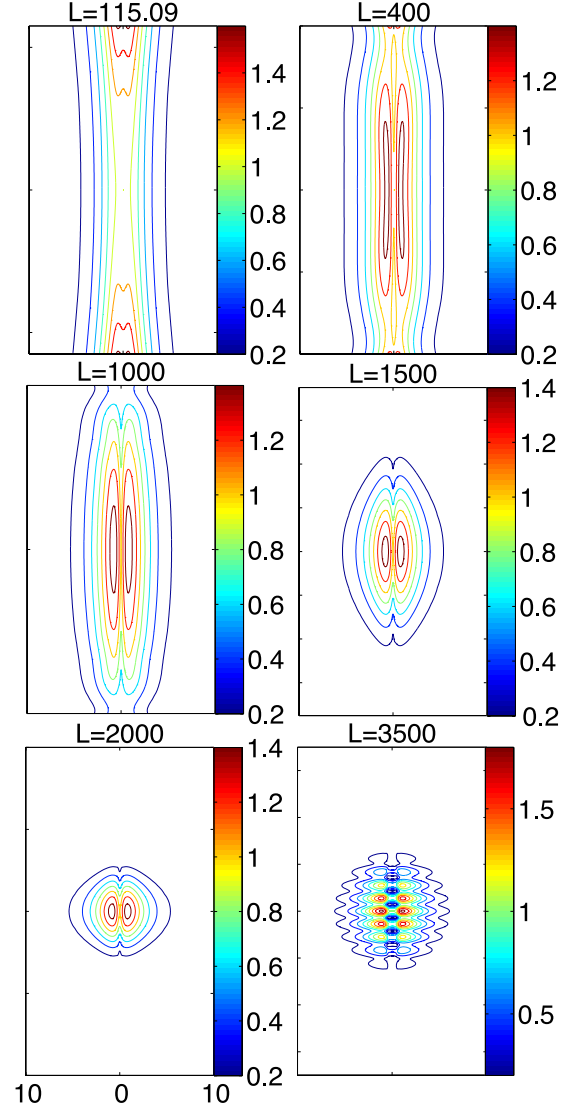


Figure 7: (Color online) The eigenfunction  $|\tilde{\psi}|$  for various  $L$ .  $\eta = 10^{-5}$ .

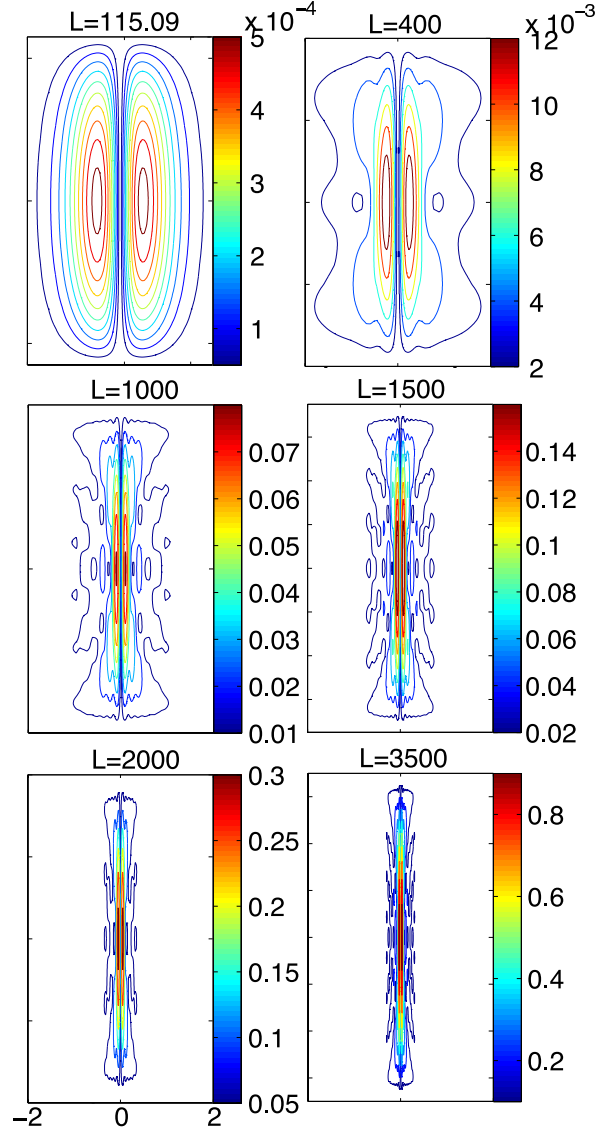


Figure 8: (Color online) The eigenfunction  $|\tilde{\phi}|$  for various  $L$  in the force-free approximation.  $\eta = 10^{-5}$ .



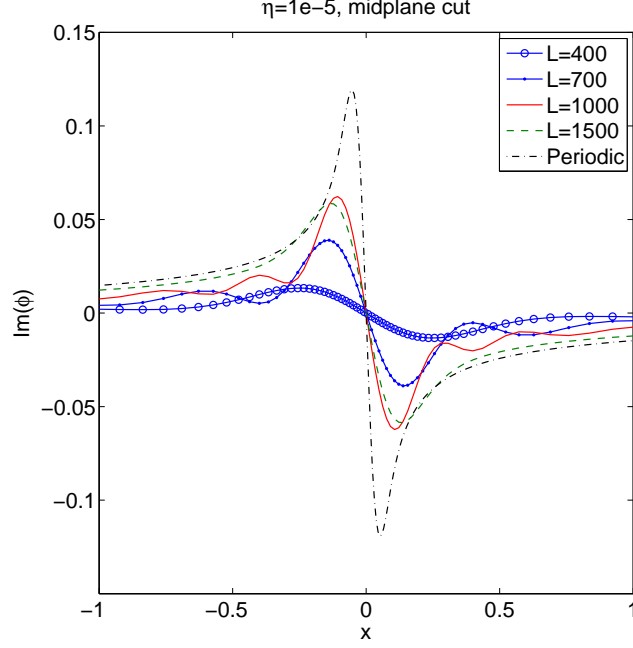


Figure 9: (Color online) The midplane cut of  $\text{Im}(\tilde{\phi})$ . Also shown is the periodic solution with  $k_z = 0$  for reference.

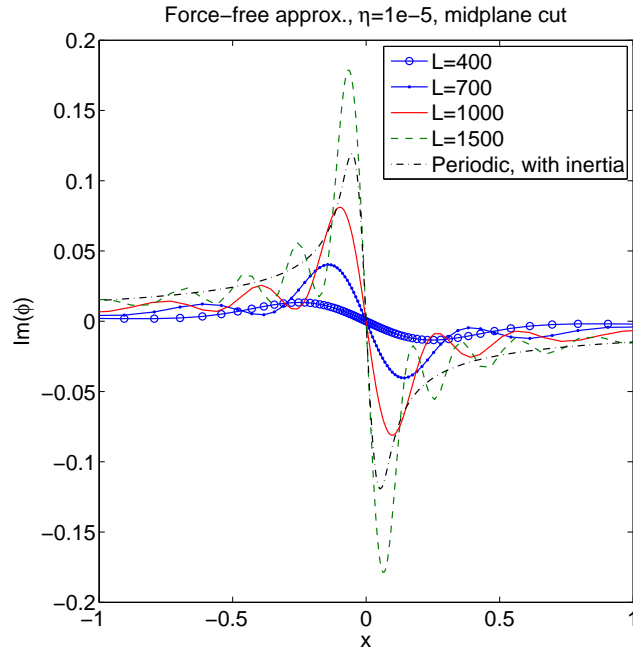


Figure 10: (Color online) The midplane cut of  $\text{Im}(\tilde{\phi})$  for the force-free approximation. Also shown is the  $k_z = 0$  periodic solution (with inertia) for reference.

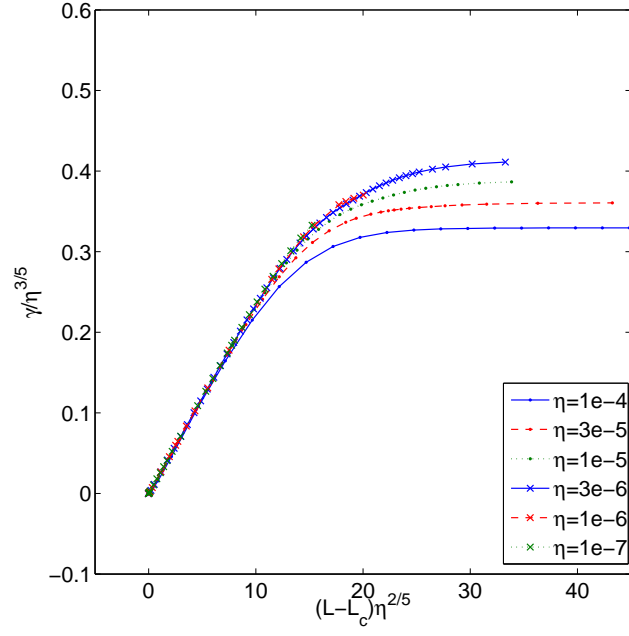


Figure 11: (Color online) Rescaled line-tied growthrate as a function of  $L$ .

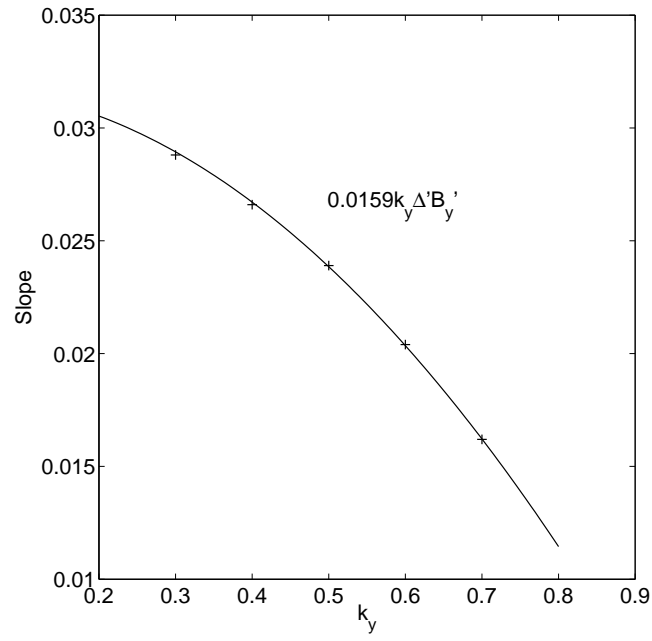


Figure 12: Slopes of the force-free  $\gamma/\eta$  versus  $L$  curve, which is approximately a straight line, for different  $k_y$ . The curve  $0.0159k_y\Delta'B_y'$  is an excellent fit with the numerical results.